



2019

Conserved Vibrational Coherence in the Ultrafast Rearrangement of 2-Nitrotoluene Radical Cation

Derrick Ampadu Boateng
VCU

Mi'Kayla D. Word
VCU

Lavrenty Gutsev
VCU, lgutsev@outlook.com

Puru Jena
Virginia Commonwealth University

Katharine M. Tibbetts
VCU, kmtibbetts@vcu.edu

Follow this and additional works at: https://scholarscompass.vcu.edu/chem_pubs

 Part of the [Chemistry Commons](#)

Downloaded from

https://scholarscompass.vcu.edu/chem_pubs/91

This Article is brought to you for free and open access by the Dept. of Chemistry at VCU Scholars Compass. It has been accepted for inclusion in Chemistry Publications by an authorized administrator of VCU Scholars Compass. For more information, please contact libcompass@vcu.edu.

Conserved Vibrational Coherence in the Ultrafast Rearrangement of 2-Nitrotoluene Radical Cation

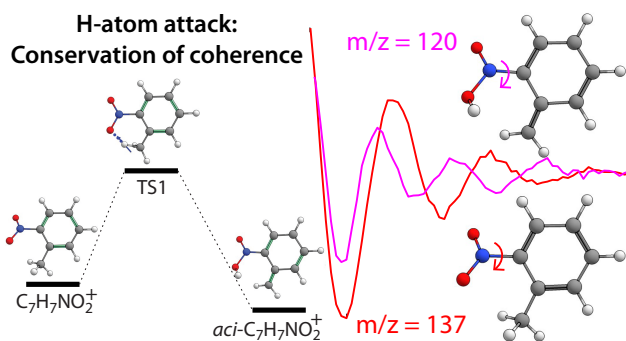
Derrick Ampadu Boateng,[†] Mi'Kayla D. Word,[†] Lavrenty G. Gutsev,[‡] Puru Jena,[‡]
and Katharine Moore Tibbetts^{*,†}

[†]*Department of Chemistry, Virginia Commonwealth University, Richmond, VA 23284*

[‡]*Department of Physics, Virginia Commonwealth University, Richmond, VA 23284*

E-mail: kmtibbetts@vcu.edu

Phone: (804)-828-7515



Abstract

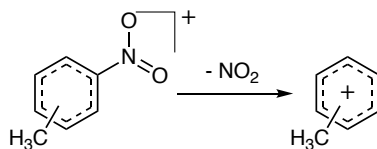
2-nitrotoluene (2-NT) is a good model for both photolabile protecting groups for organic synthesis and the military explosive 2,4,6-trinitrotoluene (TNT). In addition to the direct C–NO₂ bond-cleavage reaction that initiates detonation in TNT, 2-NT undergoes an H-atom attack reaction common to the photolabile 2-nitrobenzyl group,

which forms the *aci*-nitro tautomer. In this work, femtosecond pump-probe measurements with mass spectrometric detection and density functional theory (DFT) calculations demonstrate that the initially-prepared vibrational coherence in 2-NT radical cation (2-NT⁺) is preserved following H-atom attack. Strong-field adiabatic ionization is used to prepare 2-NT⁺, which can overcome a modest 0.76 eV energy barrier to H-atom attack to form the *aci*-nitro tautomer as soon as $\sim 20\text{--}60$ fs after ionization. Once formed, the *aci*-nitro tautomer spontaneously loses $-\text{OH}$ to form $\text{C}_7\text{H}_6\text{NO}^+$, which exhibits distinctly faster oscillations in its ion yield (290 fs period) as compared to the 2-NT⁺ ion (380 fs period). The fast oscillations are attributed to the coherent torsional motion of the *aci*-nitro tautomer, which has a significantly faster computed torsional frequency (86.9 cm^{-1}) than the 2-NT⁺ ion (47.9 cm^{-1}). Additional DFT calculations identify reaction pathways leading to the formation of the dissociation products $\text{C}_7\text{H}_6\text{NO}^+$, C_7H_7^+ , and $\text{C}_6\text{H}_6\text{N}^+$. Collectively, these results reveal a rich picture of coherently- and incoherently-driven dissociation pathways in 2-NT⁺.

1 Introduction

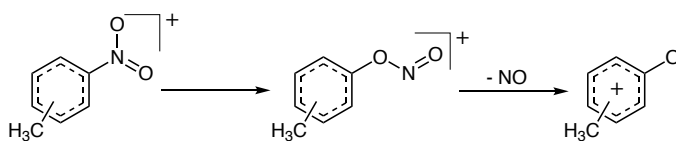
The photolabile 2-nitrobenzyl functional group has a number of applications including as a protecting group in organic synthesis,¹ as a precursor in the synthesis of DNA microarrays,² and in caged compounds for biomolecule encapsulation.³ In addition to these applications, the 2-nitrobenzyl group is found in the military explosive 2,4,6-trinitrotoluene (TNT),⁴ which has been the subject of numerous experimental⁵⁻⁸ and theoretical⁹⁻¹² investigations into its dissociation pathways. The nitrotoluene (NT) isomers 2-, 3-, and 4-NT are often used as model compounds for TNT, and their photodissociation pathways have been studied for decades using mass spectrometric detection of cationic photoproducts.^{5,13-22} These studies have demonstrated clear differences in reaction pathways of 2-NT as compared to 3- and 4-NT due to the proximity of the CH_3 and NO_2 groups in the 2-nitrotoluyly moiety.

Upon ionization, all three NT isomers undergo direct homolysis of the weak C–NO₂ bond (Scheme 1), producing the C₇H₇⁺ ion with m/z = 91 in mass spectrometry experiments.^{5,15–22} The C–NO₂ cleavage is also the primary initiator of detonation in TNT.⁹



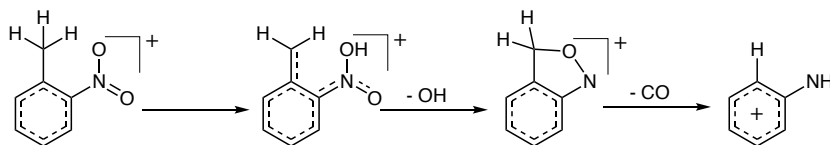
Scheme 1: C–NO₂ homolysis in NTs.

The 3- and 4-NT cations also undergo nitro-nitrite rearrangement (NNR, Scheme 2), leading to the loss of NO and the formation of C₇H₇O⁺ ions with m/z = 107.^{5,16–18,20,22} The m/z = 107 ion is formed at significantly reduced yields in 2-NT,^{5,17,18} indicating that NNR is not energetically favorable in this isomer.



Scheme 2: NNR in 3- and 4-NT.

Instead of NNR, the 2-NT cation undergoes a unique process called *aci*-rearrangement wherein the aliphatic hydrogen migrates to the nitro group, which results in the formation of an *aci*-nitro tautomer in a process called ortho attack (Scheme 3). The *aci*-nitro tautomer loses OH, forming C₇H₆NO⁺ ions with m/z = 120, which can subsequently lose CO to produce C₆H₆N⁺ with m/z = 92.^{5,13,14,16–18,21}



Scheme 3: *Aci*-rearrangement and sequential dissociation in 2-NT.

The *aci*-rearrangement reaction in neutral 2-NT was first reported in 1962²³ and was determined to be the initial step in the sequential dissociation of 2-NT cation to form m/z = 120

and $m/z = 92$ ions in 1965.¹³ More recently, theoretical studies have proposed mechanisms for this sequential dissociation pathway in neutral 2-NT²⁴⁻²⁶ and 2-NT cation²¹ in the gas phase. However, the reaction dynamics and their timescales involved are still only partially understood.

The ultrafast dynamics of the *aci*-rearrangement in neutral 2-NT and other 2-nitrobenzyl compounds have been studied in solution phase using time-resolved pump-probe experiments with femtosecond laser pulses.^{27,28} Upon excitation of 2-NT to the $\pi\pi^*$ (S_2) state, *aci*-rearrangement occurs following relaxation to the $n\pi^*$ (S_1) state on a timescale of 10 ps or after intersystem crossing to the triplet manifold on a timescale of 1300 ps.²⁷ While these experiments provide key insights into the *aci*-rearrangement dynamics in neutrals, the solution-phase timescales may be affected by solvent interactions and subsequent molecular dissociation pathways have not been explored.^{27,28} Additionally, no *aci*-rearrangement or subsequent dissociation timescales have been reported in 2-NT cation. As a result, knowledge of both the *aci*-rearrangement and subsequent dissociation mechanisms may be gained through femtosecond pump-probe measurements on the isolated 2-NT cation.

Pump-probe experiments have provided extensive insight into the dissociation dynamics of isolated organic cations including halogenated methanes,²⁹⁻³² alkyl aryl ketones³³⁻³⁶ azobenzene,^{37,38} dimethyl methylphosphonate,³⁹ and 3- and 4-NT.²² In these molecules, ionization with a strong-field femtosecond pump pulse results in the formation of a coherent superposition of vibrational states, or “wave packet,” in the ground electronic state of the cation. Wave packet excitation to a dissociative ionic excited state by the time-delayed probe pulse results in oscillations in the parent and fragment ion yields as a function of probe delay with period corresponding to the coherently excited vibrational mode.^{22,29-39} Our recent pump-probe study of 3- and 4-NT cations²² determined that wave packets are formed along an in-plane bending mode in (216 fs period, 160 cm^{-1}) 3-NT cation and the C–NO₂ torsional mode (470 fs period, 70 cm^{-1}) in 4-NT cation. Coherent excitation with the probe pulse was found to drive the C–NO₂ homolysis pathway in Scheme 1.

To answer outstanding questions about the dynamical timescales involved in H-atom attack and subsequent dissociation pathways in 2-NT, this work reports the first femtosecond pump-probe measurements on the isolated 2-NT cation. We use near-infrared (1300 nm) laser pulses for ionization because strong-field excitation with wavelengths in the range of $\sim 1200 - 1600$ nm induces predominantly adiabatic electron-tunneling ionization instead of nonadiabatic multiphoton ionization, which dominates at the Ti:Sapphire wavelength of 800 nm.^{40,41} Adiabatic ionization with near-infrared pulses has been widely used to prepare a high population of ground-electronic state polyatomic cations as vibrational wave packets,^{22,35,36,38,39} and produces significant improvements in the resolution of ion-yield oscillations in pump-probe experiments as compared to using 800 nm for ionization.^{35,39} Interpretation of the experimental dissociation dynamics is supported by a series of density functional theory (DFT) calculations of the energies, relaxation pathways, and vibrational frequencies of the 2-NT cation and its *aci*-nitro tautomer, along with molecular dynamics simulations to estimate the timescale of H-atom attack. We will show that coherent torsional wave packet motion is conserved following H-atom attack, with the *aci*-nitro tautomer of 2-NT cation producing distinct dynamics in the $-OH$ loss product at $m/z = 120$ as compared to other ions. These results open up the possibility of coherent control over the reactions of photolabile 2-nitrobenzyl protecting groups.

2 Methods

2.1 Experiment

Portions of the experimental setup have been described in detail in our previous publications;^{22,39,42,43} here we describe the modifications to produce tunable probe pulses in the visible range. A commercial Ti:Sapphire regenerative amplifier (Astrella, Coherent, Inc.) producing 30 fs, 800 nm, 2.2 mJ pulses is used to pump an optical parametric amplifier (OPA, TOPAS Prime) to produce 1200 – 1600 nm, 20 fs, 300 μJ pulses. Figure 1 shows

a schematic diagram of the beam paths. A 50:50 (r:t) beam splitter placed after the OPA output splits the beam into pump and probe lines. The pump beam passes through a $\lambda/2$ wave plate and Wollaston polarizer for attenuation and is then expanded by a telescope made of spherical mirrors with $f = -10$ cm and $f = 50$ cm to increase the beam diameter (measured with the knife-edge method) from 4.5 mm to 22.0 mm. The expanded beam has maximum energy ranging from 50 – 150 μJ depending on the wavelength, and can reach focal peak intensities exceeding $4 \times 10^{14} \text{ W cm}^{-2}$.⁴³ The probe beam is directed to a retro-reflector placed on a motorized translation stage (ThorLabs, Inc), attenuated with a variable neutral density filter, and frequency-doubled with a β -barium borate (BBO) crystal. The maximum probe energy is 10 μJ at 650 nm. With a home built frequency-resolved optical gating (FROG) setup,⁴⁴ the duration of the pump and probe were measured to be 18 fs and 25 fs, respectively (Supporting Information, Figure S1). Pump and probe beams are recombined on a dichroic mirror and focused with a $f = 20$ cm fused silica biconvex lens into an ultrahigh vacuum chamber (base pressure 2×10^{-9} torr) coupled to a custom-built linear time-of-flight mass spectrometer (TOFMS) described previously.^{42,43}

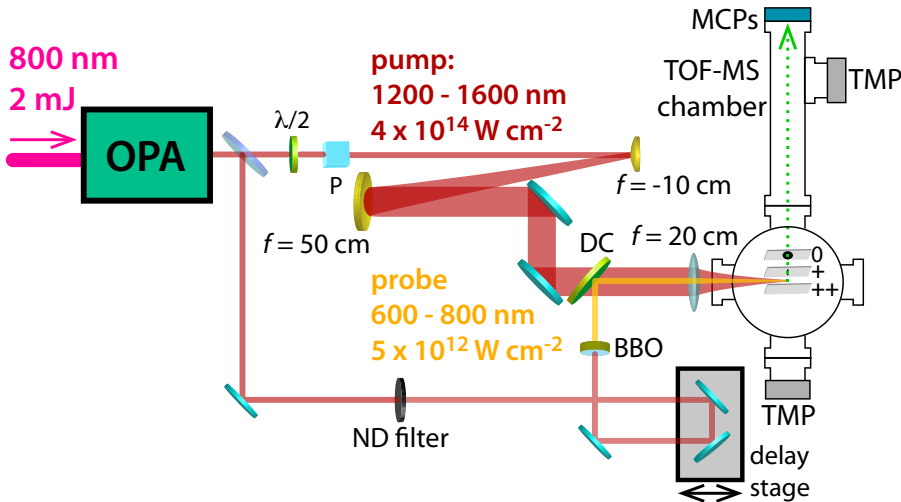


Figure 1: Schematic of pump and probe beam paths. $\lambda/2$: half wave plate; P: Wollaston polarizer; ND: neutral density; BBO: β -barium borate crystal; DC: dichroic mirror.

Pump-probe measurements on 2-NT were taken with a pump wavelength of 1300 nm at intensities of $1 \times 10^{14} \text{ W cm}^{-2}$ and $2 \times 10^{14} \text{ W cm}^{-2}$, as determined by the yield of Xe^{n+}

ions using the method of Hankin.⁴⁵ The 650 nm probe intensity was determined through measurement of the energy using a pyroelectric power meter (PM-USB, Coherent, Inc.) and the beam waist using a CMOS camera (DCC1645M, ThorLabs, Inc.). The beam waist and Rayleigh range are 38 μm and 10 mm, respectively (Supporting Information, Figure S2), producing estimated peak intensities ranging from $9 \times 10^{11} - 5 \times 10^{12} \text{ W cm}^{-2}$ at pulse energies of 1 – 6 μJ . The pump-probe delay was scanned from -500 fs (probe before pump) to $+8000 \text{ fs}$ in steps of 20 fs. The 2-NT sample (99%, Sigma-Aldrich) is used without further purification and introduced into the TOFMS at a pressure of $1.2 \times 10^{-7} \text{ torr}$ measured near the microchannel plate (MCP) detector. Mass spectra of 2-NT taken at each pump-probe delay and averaged over 1000 laser shots were recorded with a 1 GHz digital oscilloscope (LeCroy WaveRunner 610Zi). The reported transient ion signals were obtained from averaging 40 pump-probe scans taken over three days.

2.2 Theory

Our density functional theory (DFT) calculations were conducted using Gaussian 16 suite of programs.⁴⁶ The 6-311+G* (5s4p1d) basis set⁴⁷ was initially used for all atoms, and subsequent calculations with the the larger CBSB7 basis set⁴⁸ were performed to evaluate the energies. The total energy threshold was 10^{-8} a.u. from the convergence threshold that was set to 10^{-3} eV/\AA .

We used the BPW91⁴⁹ functional for preliminary geometry and ground-state energy calculations, which is in the generalized gradient approximation (GGA) family. After these preliminary calculations, neutral and cation geometries were optimized with the hybrid functionals B3LYP,^{50,51} CAM-B3LYP,⁵² and ωB97XD ,⁵³ along with the Møller-Plesset perturbation theory method truncated at second order (MP2).⁵⁴ The calculated neutral and cation energies, along with comparison to the literature at the CBS-QB3 level and VUV photoionization experiments²¹ are given in Table 1. It is notable that the dispersion-corrected meta-GGA exchange functionals ωB97XD and CAM-B3LYP predict vertical ionization potentials

that agree to within 0.05 eV with the recently reported experimental value of 9.43 eV.²¹ The neutral, cation, and *aci*-tautomer geometries are given in the Supporting Information, Figure S3 and Tables S1 and S2. The harmonic vibrational frequencies obtained from these calculations are tabulated in the Supporting Information, Tables S3–S5.

Table 1: Calculated energies of 2-NT and comparison to literature. *a* Ref.²¹

method	neutral (Hartree)	cation (Hartree)	IP _{vert} (eV)
BPW91	-476.011304	-475.677837	9.074
B3LYP	-476.046909	-475.703077	9.356
CAM-B3LYP	-475.814173	-475.465865	9.478
ω B97XD	-475.878995	-475.531522	9.455
MP2	-474.688852	-474.329081	9.790
CBS-QB3 ^a	-475.311340	-474.959199	9.582
Expt. ^a			9.43

To determine the excited-state energies of the 2-NT neutral and cation, we performed time-dependent DFT (TDDFT) calculations⁵⁵ to obtain the simulated optical spectrum of each species. We calculated the first 100 singlet-singlet (for neutral 2-NT) and doublet-doublet (for 2-NT cation) transitions with four different functionals: BPW91, B3LYP, CAM-B3LYP and ω B97XD. Tabulated results for lowest 12 neutral 2-NT energies and 23 lowest cation energies, along with oscillator strengths, are given in the Supporting Information, Tables S6–S7. The simulated spectra for neutral 2-NT superimposed on the experimental spectrum obtained from NIST⁵⁶ are shown in Figure 2(a). As with the predicted IP_{vert} values, the predicted excited state energies computed with the ω B97XD and CAM-B3LYP functionals agree very well with one another and capture the strong absorption feature centered around 4.9 eV in the experimental spectrum. The excitation energies and oscillator strengths for the 2-NT cation shown in Figure 2(b) suggest that the lowest-lying accessible excited state lies at approximately 1.8–1.9 eV and that the next state lies at approximately 3.2–3.4 eV. Based on these results, the probe wavelength was set at 650 nm (1.9 eV) for the experiments. The experimental probe spectrum is shown as the orange shaded region in Figure 2(b). This probe spectrum and the associated 1300 nm pump wavelength were used

for all experimental measurements presented below.

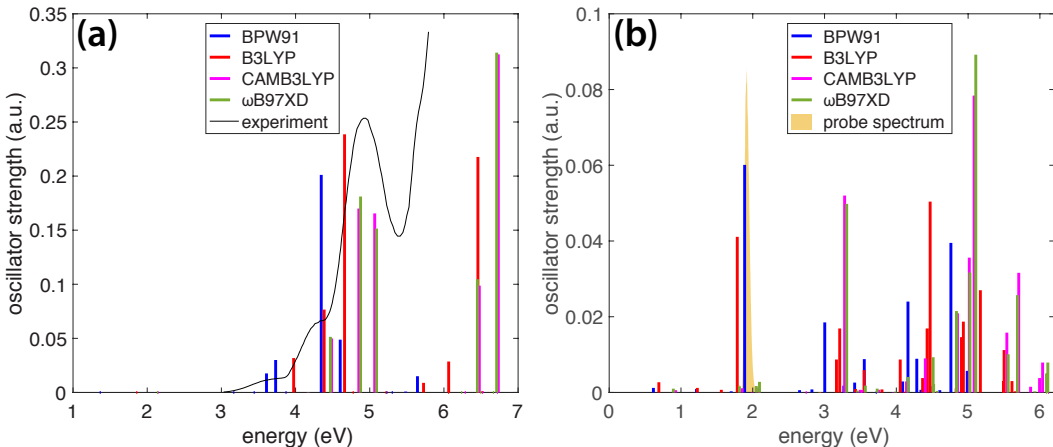


Figure 2: (a) TDDFT spectra for neutral 2-NT. Experimental spectrum obtained from NIST.⁵⁶ (b) TDDFT spectra for 2-NT cation. The probe spectrum is shown as the orange shaded region. Spectra were computed using the BPW91 (blue), B3LYP (red), CAMB3LYP (magenta), and ω B97XD (green) functionals with the 6-311+G* basis.

The transition states of the hydrogen transfer in *aci*-rearrangement were prepared via displacements of the hydrogen atoms. The transition states of rotations and bond-breaking were scanned for using a Modredundant scan in Gaussian 16. The geometries found at the energetic cusps were then optimized using the Berny Algorithm. Using vibrational frequency calculations, these states were confirmed to correlate to first order saddle points because each transition state had one imaginary frequency with the imaginary mode vectors. To confirm the validity of the transition states found, synchronous transit-guided quasi-Newton (STQN)⁵⁷ calculations were performed with and without initial guesses (QST3 and QST2 respectively). To ensure that no transition state was missed, we used the transition state already found as the starting or ending point for the QST calculations. The proposed pathways were then justified using full internal reaction coordinate (IRC)⁵⁸ pathways. Energies for the reaction pathways using the ω B97XD/CBSB7 combination of exchange functional and basis sets are reported. Lastly, 100 *ab initio* molecular dynamics runs using the ADMP method⁵⁹ with 0.1 fs time-steps and 280 fs duration were performed to determine the time required for the *aci*-rearrangement. In ADMP calculations, the forces between atoms are

calculated via DFT (in our computations using the BPW91 functional) while the velocities are propagated classically. These simulations were initiated from the transition state for the H-atom attack and included all post ionization relaxation energy (differences in vertical and adiabatic energies of 0.1951 eV) in the imaginary mode.

3 Results and Discussion

The experiments and calculations presented here demonstrate the surprising result that vibrational coherence in 2-NT cation is preserved after it undergoes spontaneous H-atom attack to form the *aci*-nitro tautomer. This finding is the first (to the best of our knowledge) report of preserved vibrational coherence following an intramolecular rearrangement reaction **in a radical cation**, and builds on recent reports of preserved vibrational coherence in the radical cations of azobenzene³⁸ and *N*-methyl morpholine^{60,61} following internal conversion. The determination of vibrational coherence preservation rests on the experimental and theoretical results presented in this section, which paint a complex picture of both coherent and incoherent excitation pathways leading to the dissociation of the 2-NT cation.

This section is organized as follows: First, we present the pump-probe mass spectrometry results (3.1), followed by a detailed analysis of the observed oscillatory ion-yield dynamics (3.2). Next, we present the computed reaction pathways leading to the formation of $C_7H_7^+$, $C_7H_6NO^+$, and $C_6H_6N^+$ (3.3). We then discuss the experimental and theoretical evidence for coherent vibrational motions of the *aci*-nitro tautomer (3.4). Finally, we present a full picture of the coherent and incoherent dissociation pathways in 2-NT⁺ (3.5).

3.1 Pump-probe measurements

Figure 3(a) shows the mass spectra of 2-NT taken with 1300 nm, 18 fs, 2×10^{14} W cm⁻² pump pulses and 650 nm, 25 fs, 5×10^{12} W cm⁻² probe pulses at pump-probe delays $\tau = -500$ fs (bottom) and $\tau = +4000$ fs (middle), as well as their difference (top). At negative

delay, the largest peaks in the mass spectrum are the parent 2-NT cation at $m/z = 137$ (highlighted in red) and the OH loss product $C_7H_6NO^+$ at $m/z = 120$ (magenta). Because the probe is non-ionizing, the ion signal is exclusively due to the 1300 nm pump pulse. The large yield of parent 2-NT⁺ as compared to previously reported mass spectra taken with femtosecond lasers^{5,17,18} is consistent with the expected adiabatic ionization process at 1300 nm excitation.^{22,35,36,38–41} At positive delay, a decrease in the $m/z = 137$ and $m/z = 120$ peaks accompanied by an increase in the peaks corresponding to the smaller ions at $m/z = 92$ (green), $m/z = 91$ (blue), $m/z = 77$ (orange), and $m/z = 65$ (cyan) is observed. Based on previous reports,^{5,13,14,16–18,21} these m/z values are assigned as to the following ions: $C_6H_6N^+$ (92), $C_7H_7^+$ (91), $C_6H_5^+$ (77), and $C_5H_5^+$ (65). The increase in these fragment ion yields at the expense of the parent ion indicates that they are formed via excitation of the parent 2-NT⁺ by the 650 nm probe pulse.^{22,29–39}

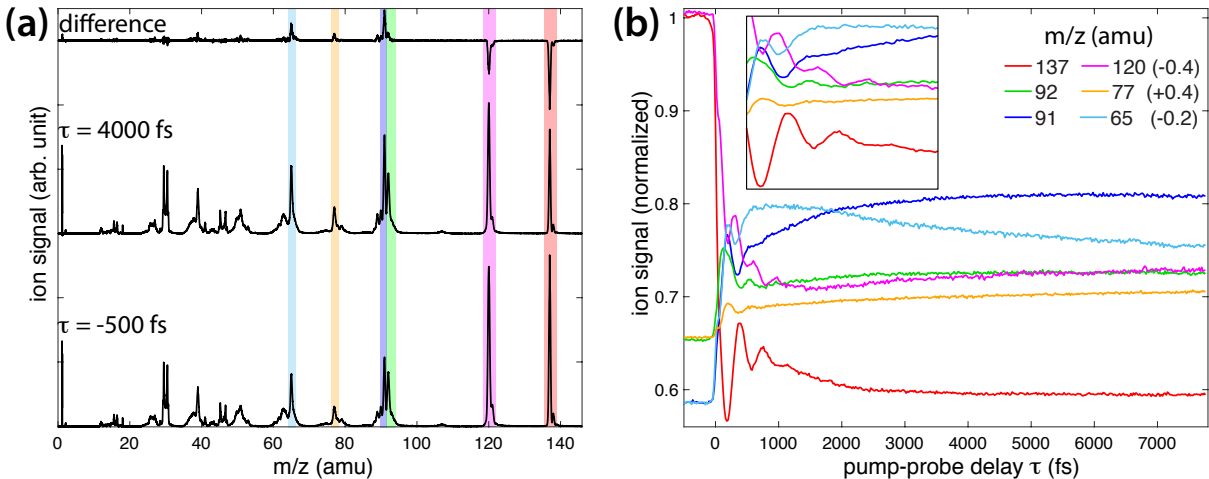


Figure 3: (a) Mass spectra of 2-NT taken at $\tau = -500$ fs and $\tau = 4000$ fs, along with their difference. (b) Transient ion signals as a function of pump probe delay. The inset magnifies the region from 50 – 1500 fs.

Figure 3(b) shows the transient ion signals highlighted in panel (a) as a function of pump-probe delay τ , with all signals normalized to the signal of the parent 2-NT⁺ at negative time-delay. The $m/z = 120$, 77, and 65 signals have been shifted on the ordinate axis by -0.4, +0.4, and -0.2 units, respectively, for clarity. The inset in Figure 3(b) magnifies the region from

50 – 1500 fs showing the oscillating ion signals that indicate coherent vibrational dynamics. At short delay times, the oscillations in the $m/z = 137$ and 120 ions are roughly out-of-phase with the oscillations of the smaller fragment ions, consistent with coherent excitation by the probe pulse.^{22,29–39} The same transient dynamics with smaller-amplitude features were observed for lower pump and probe intensities (Supporting Information, Figure S4).

3.2 Analysis of oscillatory dynamics

The ~ 380 fs oscillation period in the 2-NT ion signals is of similar magnitude to oscillation periods in the related molecules 4-NT (470 fs),²² acetophenone (650 fs),^{33,35,36} and 4-methylacetophenone (730 fs).³⁴ In the latter molecules, the oscillations were attributed to the torsional motion of the nitro or acetyl substituent with respect to the benzene ring, due to the relaxation of the cation from the planar neutral geometry to the non-planar optimized geometry.^{22,33–36} Our ω B97XD/CBSB7 calculations indicate that the C–NO₂ torsional angle of 26.0° in neutral 2-NT shifts to 35.5° at the optimized cation geometry (Figure 4), suggesting that the torsional vibrational mode can be excited upon ionization. The torsional angle for neutral 2-NT is in reasonable agreement with previous theoretical results at the PBE0/6-31+G level reporting an angle of 19.4° ²⁵ and within the magnitude of the estimated equilibrium torsional angle of $35 \pm 15^\circ$ relative to planar geometry obtained by gas-phase electron diffraction measurements.⁶² The calculated vibrational frequency of the torsional mode (shown in Figure 4) ranged from $45.0 - 65.7 \text{ cm}^{-1}$ in neutral 2-NT and $31.9 - 57.1 \text{ cm}^{-1}$ in 2-NT⁺, depending on the method (Supporting Information, Tables S4 – S5). The slower predicted oscillation periods of 580 – 1200 fs as compared to the observed 380 fs (88 cm^{-1}) can be explained by the inherent uncertainty of $\sim 30 - 100 \text{ cm}^{-1}$ in the computed values; a similar under-estimation of the torsional frequency was found for the 4-NT cation in our previous work.²² We also note that the out-of-plane ring-bending mode calculated at $89.7 - 105.8 \text{ cm}^{-1}$ in 2-NT⁺ is unlikely to contribute to the observed oscillations because the ring geometry remains planar upon ionization of 2-NT to 2-NT⁺ (Figure 4). Based on these

observations, we assign the coherent dynamics to the torsional mode.

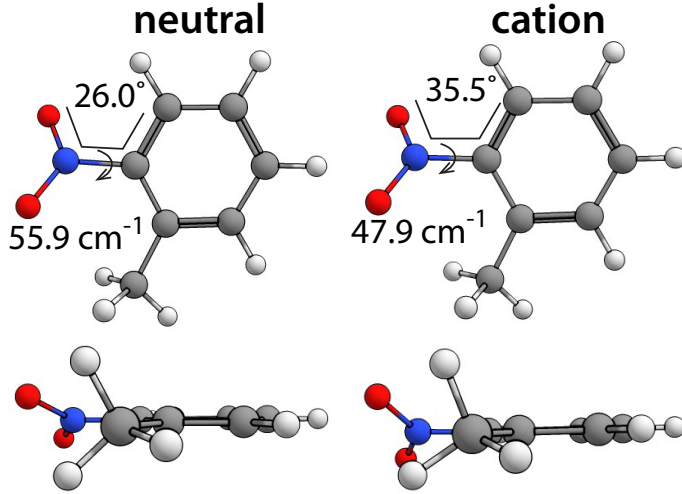


Figure 4: Neutral and ion geometries of 2-NT shown in two orientations with torsional angles and frequencies labeled.

The coherent dynamics may be analyzed in more detail by fitting the signals $S(\tau)$ for the parent 2-NT⁺ ($C_7H_7NO_2^+$) and the dissociation products highlighted in Figure 3 to the equation

$$S(\tau) = ae^{-\tau/T_1} \cos\left(\frac{2\pi}{t}\tau + \phi\right) + be^{-\tau/T_2} + ce^{-\tau/T_3} + d \quad (1)$$

where a , b , and c are amplitude coefficients, t is the oscillation period, T_1 is the coherence lifetime, T_2 is a second incoherent lifetime, T_3 is a third incoherent lifetime, and d is the final ion yield as $\tau \rightarrow \infty$. Each transient signal was fit to eq (1) using nonlinear least-squares curve fitting in MATLAB. Figure 5 shows the transient ion signals at $\tau > 40$ fs (dots) fit to eq (1): $C_7H_7NO_2^+$ (red), $C_6H_6N^+$ (green), and $C_6H_5^+$ (orange) in Figure 5(a); $C_7H_7^+$ (blue), $C_5H_5^+$ (cyan), and $C_7H_6NO^+$ (magenta) in Figure 5(b). For each transient signal, the fit components corresponding to the coherent T_1 decay (thick solid lines), T_2 decay (dashed lines), and T_3 decay (dotted lines) are shown in addition to the full fit function (black lines). The $C_7H_7NO_2^+$, $C_5H_5^+$, $C_7H_6NO^+$, and $C_6H_6N^+$ transients required the additional T_3 decay, while the $C_7H_7^+$ and $C_6H_5^+$ transients required only two decay time constants.

The coefficients extracted from curve fitting to each transient in Figures 5(a) and 5(b)

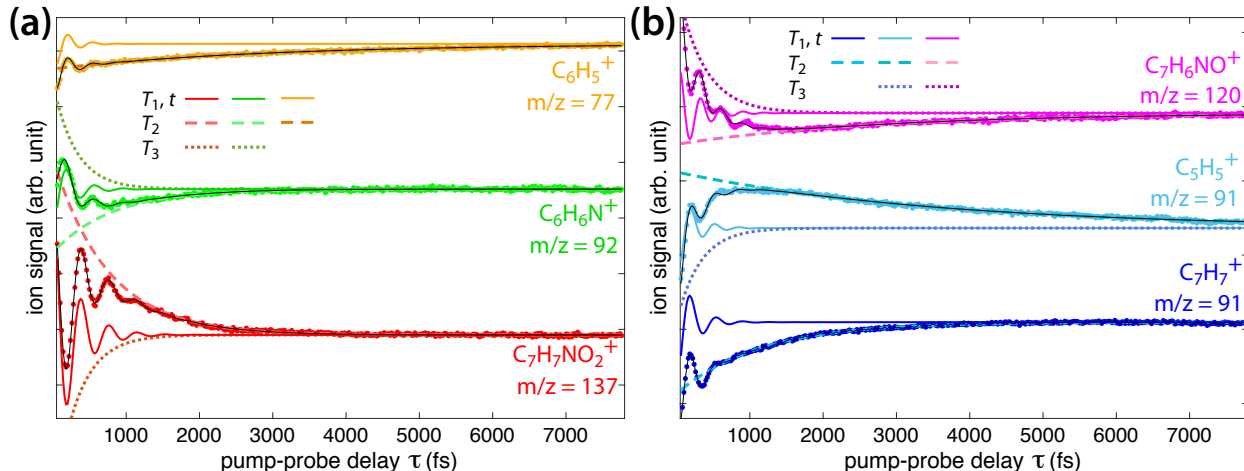


Figure 5: Transient signals (dots) of (a) $C_7H_7NO_2^+$ (red), $C_6H_6N^+$ (green), $C_6H_5^+$ (orange), and (b) $C_7H_7^+$ (blue), $C_5H_5^+$ (cyan), $C_7H_6NO^+$ (magenta). All transients are shown with fits to eq 1 (black lines) and individual components (thick solid, dashed, and dotted lines).

are given in Tables 2 and 3, respectively. All transient signals have coherent lifetimes (T_1) between approximately 200 and 300 fs, similar to the lifetimes found in 3-NT and 4-NT.²² In Table 2, the oscillation periods (t) are nearly identical for the parent $C_7H_7NO_2^+$ (382 fs) and $C_6H_6N^+$ transients (386 fs), and their phases are roughly π radians out-of-phase. In contrast, Table 3 shows a significantly shorter period of 290 fs for $C_7H_6NO^+$, and its phase is offset from that of the $C_7H_7NO_2^+$ transient by $\pi/4$ radians. The remaining excited-state products $C_6H_5^+$, $C_5H_5^+$, and $C_7H_7^+$ exhibit oscillation periods and phases in between these two extremes. Also of note are the similar T_3 values in $C_7H_7NO_2^+$, $C_7H_6NO^+$, $C_6H_6N^+$, and $C_5H_5^+$, indicating an incoherent excitation process linking these four transients.

Table 2: Coefficients extracted from fitting transient ion signals in Figure 5(a) to eq (1).

eq (1)	$C_7H_7NO_2^+$	$C_6H_6N^+$	$C_6H_5^+$
a	0.124 ± 0.003	0.037 ± 0.004	0.025 ± 0.003
T_1 (fs)	288 ± 7	244 ± 36	188 ± 19
t (fs)	382 ± 2	386 ± 13	338 ± 13
ϕ (rad)	-0.17 ± 0.03	3.12 ± 0.16	2.23 ± 0.14
b	0.149 ± 0.029	-0.066 ± 0.031	-0.0225 ± 0.0005
T_2 (fs)	760 ± 40	720 ± 120	2930 ± 150
c	-0.15 ± 0.02	0.10 ± 0.03	—
T_3 (fs)	317 ± 31	322 ± 63	—
d	0.594 ± 0.001	0.725 ± 0.001	0.296 ± 0.001

Table 3: Coefficients extracted from fitting transient ion signals in Figure 5(b) to eq (1).

eq (1)	$C_7H_6NO^+$	$C_5H_5^+$	$C_7H_7^+$
a	0.072 ± 0.004	0.065 ± 0.006	0.087 ± 0.005
T_1 (fs)	260 ± 17	212 ± 20	210 ± 11
t (fs)	291 ± 3	330 ± 10	361 ± 5
ϕ (rad)	-0.95 ± 0.08	2.45 ± 0.17	2.91 ± 0.15
b	-0.040 ± 0.002	0.076 ± 0.002	-0.096 ± 0.001
T_2 (fs)	2890 ± 480	3580 ± 280	1100 ± 20
c	0.174 ± 0.003	-0.127 ± 0.004	–
T_3 (fs)	359 ± 14	319 ± 19	–
d	1.131 ± 0.001	0.937 ± 0.001	0.809 ± 0.001

To assess the potential significance of the distinct oscillation periods across the transient ions extracted from curve-fitting, the T_2 and T_3 components of eq 1 were subtracted off from each transient ion signal and the residuals plotted in Figure 6(a). The dashed lines at 190 fs, 570 fs, and 950 fs indicate minima in the yield of $C_7H_7NO_2^+$ (red), showing a constant period of 380 fs. Both the $C_6H_6N^+$ (green) and $C_6H_5^+$ (orange) transients exhibit almost perfectly antiphase oscillations with the parent ion, indicating their formation from its coherent excitation. The $C_7H_7^+$ transient (blue) oscillations are also almost antiphase with the $C_7H_7NO_2^+$, although the first $C_7H_7^+$ minimum at 370 fs is approximately 10 fs ahead of the first $C_7H_7NO_2^+$ maximum at 380 fs. The dotted lines at 180 fs, 470 fs, and 780 fs indicate minima in the $C_7H_6NO^+$ yield, indicating that the oscillation period *increases* from 290 fs between the first and second minima to 310 fs between the second and third minima. These distinct oscillatory dynamics indicate that a different structure gives rise to the $C_7H_6NO^+$ oscillations as compared to the parent $C_7H_7NO_2^+$ oscillations. The $C_5H_5^+$ signal (cyan) exhibits oscillations that are not perfectly out-of-phase with either the $C_7H_7NO_2^+$ or $C_7H_6NO^+$ transients: its first minimum at 340 fs is 40 fs ahead of the $C_7H_7NO_2^+$ maximum and 20 fs behind the first $C_7H_6NO^+$ maximum at 320 fs. These results suggest that $C_5H_5^+$ can be formed by excitation of both the $C_7H_7NO_2^+$ and $C_7H_6NO^+$ precursor structures.

Fast Fourier Transform (FFT) of the oscillatory signals from 60 – 3000 fs in Figure 6(a) are shown in Figure 6(b). The well-resolved peak in the $C_7H_7NO_2^+$ signal (red) at 91 cm^{-1}

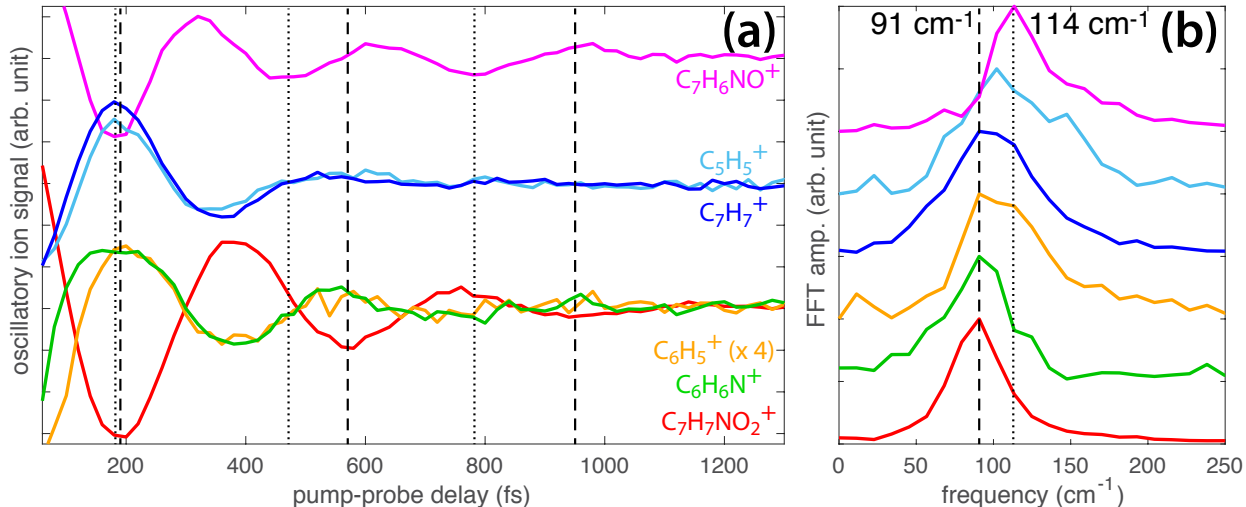


Figure 6: (a) Oscillatory components of the transient ion signals of $C_7H_7NO_2^+$ (red), $C_6H_6N^+$ (green), $C_7H_7^+$ (blue), and $C_7H_6NO^+$ (magenta). Dashed and dotted lines denote minima in $C_7H_7NO_2^+$ and $C_7H_6NO^+$, respectively. (b) FFT of signals in (a).

(367 fs period) indicated by the dashed line agrees with the 383 fs oscillation period obtained from fitting to eq (1). The $C_6H_6N^+$ (green), $C_6H_5^+$ (orange), and $C_7H_7^+$ (blue) signals also show this peak, although the peaks are somewhat broadened in $C_6H_5^+$ and $C_7H_7^+$. In contrast, the $C_7H_6NO^+$ peak (magenta) is clearly up-shifted to 114 cm^{-1} (293 fs period) indicated by the dotted line, with a long tail extending to the higher frequencies. The asymmetrical peak is consistent with the slowing oscillation period observed in Figure 6(a). The distinctly higher frequency for $C_7H_6NO^+$ provides further evidence that the structure giving rise to these oscillations is distinct from the parent $2NT^+$. The $C_5H_5^+$ (cyan) peak is also up-shifted from the $C_7H_7NO_2^+$ frequency, providing further evidence that it can be formed from both the parent $2NT^+$ and the $C_7H_6NO^+$ precursor structure. In order to rationalize the observation of two distinct coherently excited structures in our pump-probe data, we present results of computed reaction pathways in $2-NT^+$ in Section 3.3 and then propose that the oscillations in the $C_7H_6NO^+$ yield may be attributed to coherent motion and relaxation of the *aci*-nitro tautomer of $2-NT^+$ in Section 3.4.

3.3 Computed reaction pathways in 2-NT⁺

We now consider the reaction pathways that lead to the formation of the 2-NT⁺ fragmentation products C₇H₇⁺, C₇H₆NO⁺, and C₆H₆N⁺. All computational results were performed with the ω B97XD/CBSB7 method.

3.3.1 Direct C–NO₂ bond homolysis: Formation of C₇H₇⁺

The similar oscillation periods and offset phases of the C₇H₇NO₂⁺ and C₇H₇⁺ transients (Tables 2, 3 and Figure 6) suggest that coherent excitation of the parent molecular ion results in C–NO₂ homolysis to form C₇H₇⁺, as was observed in 3-NT and 4-NT.²² Computation of this dissociation pathway revealed no transition state and formation of C₇H₇⁺ in the singlet and triplet states at 10.98 eV and 11.69 eV, respectively (Figure 7). The singlet dissociation energy is in good agreement with recent VUV photoionization experiments giving an appearance energy for C₇H₇⁺ at 11.01 ± 0.03 eV and calculations at the CBS-QB3 level indicating dissociation at 11.17 eV.²¹ The 1.9 eV probe pulse (orange arrow, Figure 7) can easily exceed the dissociation barrier to singlet C₇H₇⁺ formation but doesn't exceed the barrier for triplet formation, suggesting that the observed C₇H₇⁺ is formed exclusively in the singlet state.

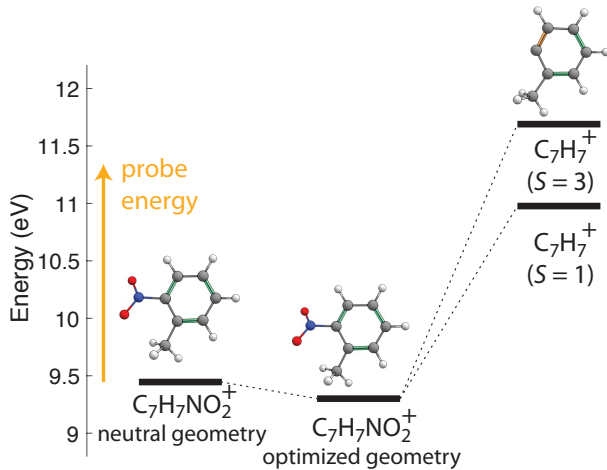


Figure 7: Mechanism of -NO₂ loss from 2-NT⁺ showing the energy required to form C₇H₇⁺ in both singlet ($S = 1$) and triplet ($S = 3$) states. The probe photon energy is shown to scale (orange arrow).

3.3.2 H-atom attack and OH loss: Formation of $C_7H_6NO^+$

The high yield of $C_7H_6NO^+$ in our mass spectra at negative time-delay (i.e., in the absence of the probe pulse) indicates that the parent $2NT^+$ can spontaneously undergo *aci*-rearrangement via H-atom attack and lose OH on the $\sim\mu s$ flight time in the TOF-MS, consistent with previous mass spectrometry studies.^{5,13,14,16–18,21} According to our computations of the *aci*-rearrangement reaction pathway (Figure 8), the reaction has an activation barrier of 0.76 eV from the vertical IP of 9.45 eV. This energy is lower than the pump photon energy (0.95 eV at 1300 nm), which suggests that absorption of an additional pump photon during the ionization process can provide the necessary energy to initiate the H-atom attack. Once TS1 is reached and the hydrogen transfers to the nitro oxygen (INT1 in Figure 8), a series of rotations (TSr, Int1r, and TSr2 in Figure 8) result in the most stable *aci*-nitro tautomer INT2 at 8.62 eV.

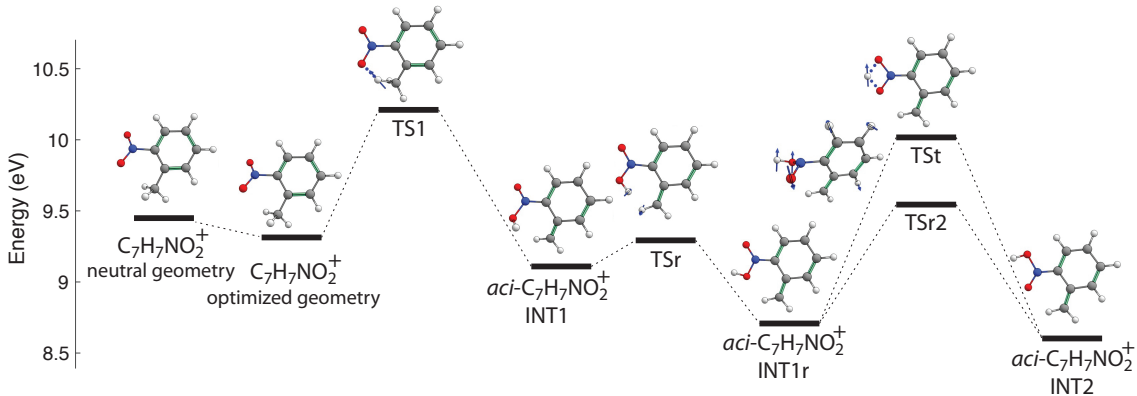


Figure 8: Mechanism of *aci*-rearrangement in $2NT^+$ computed at the $\omega B97XD/CBSB7$ level.

This mechanism generally agrees with the recently reported pathway computed at the CBS-QB3 level with the 6-311G basis,²¹ with three notable exceptions. First, the 10.22 eV energy of the transition state TS1 is 0.2 eV higher than the CBS-QB3 value. Second, the final transition state TSr2 was not reported in the CBS-QB3 results, but rather the transition state TSst, which was reported to be the highest-energy transition state in the pathway at 10.16 eV (compared to 10.01 eV in our calculations). Third, the *aci*-nitro tautomer INT2

was reported to be 0.38 eV higher at 9.00 eV. These discrepancies are likely due to the use of a composite method to compute energies with DFT-optimized geometries in Ref.,²¹ in contrast to the use of a consistent DFT method to optimize both the geometries and energies in the present calculations. Furthermore, all transition states in our computations were verified with IRC pathway calculations. The corresponding structures (Supporting Information, Figure S5) clearly show the displacement vectors in each transition state.

To estimate the time needed for H atom transfer to the nitro oxygen, ADMP trajectories were computed beginning from TS1 with the excess energy of 0.195 eV from cation relaxation. The zero point vibrational energy (ZPVE) was also included and partitioned among the non-imaginary vibrational modes using microcanonical sampling. Hydrogen transfer was measured using the bond radii R(11-14) (C–H) and R(14-17) (O–H) (Figure 9). The average times required to reach TS1 and INT1 from the optimized 2-NT⁺ geometry obtained by these calculations (Figure 9) indicate that the INT1 *aci*-nitro tautomer structure can be accessed **as soon as** 20.8 ± 5.9 fs. The average trajectories for the forward (from TS1 to INT1) and reverse (from TS1 to 2NT⁺) hydrogen motions leading to the computed reaction times are given in the Supporting Information, Figure S6. Continued simulation of the forward reaction out to 500 fs found that the average time required to access the next transition state TSr is 145 ± 75 fs. **Because the ADMP trajectories were initiated from TS1, the computed 21 fs timescale likely represents a lower limit on the reaction time. A more reasonable timescale is on the order of ~ 60 fs, which was observed for intramolecular H-atom attack reactions in excited-state methyl salicylate⁶³ and 2-(2'-hydroxyphenyl)benzothiazole.⁶⁴ The excited-state dynamics leading to such rapid H-atom attack in the latter works also suggests that the reaction in 2-NT cation may occur on an excited state PES, although future computational studies will be needed to test this hypothesis. Nevertheless, the calculations suggest that some population of *aci*-nitro tautomer as structure INT1 is likely present by the time the coherent oscillations are observable beginning at ~ 100 fs (c.f., Figure 6), while the structure's relaxation to the stable structure INT2 is expected to proceed over the next several hundred**

femtoseconds. As will be discussed below in Section 3.4, both the H-atom transfer and relaxation timescales are consistent with the observed oscillations in the $C_7H_6NO^+$ transient arising from coherent torsional motion of the *aci*-nitro tautomer.

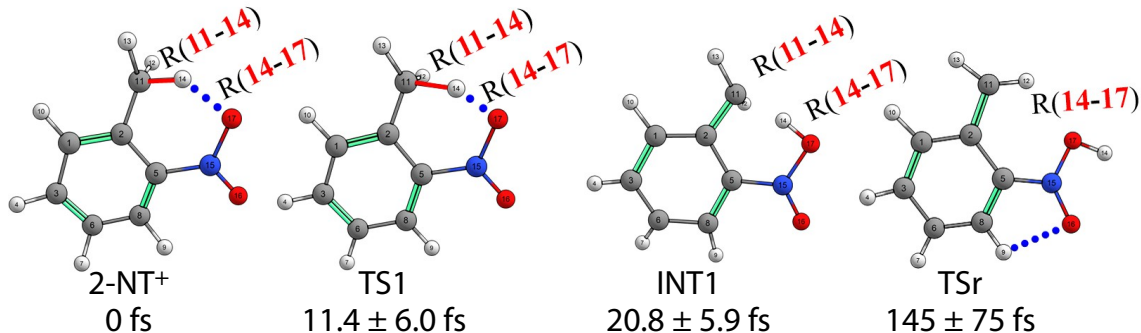


Figure 9: Structures involved in the H atom transfer to the nitro oxygen, along with average times required to reach them.

We next consider pathways to OH loss and formation of $C_7H_6NO^+$ beginning from INT2 (Figure 10 and Supporting Information, Figure S7). The most favorable pathway leads to $C_7H_6NO^+$ in the singlet state, and involves first cyclization (TS2 and INT3) followed by OH cleavage to produce $C_7H_6NO^+$ (P2, $S = 1$, Figure 10). Because the energy of P2 (9.63 eV, in good agreement with the 9.65 eV reported with CBS-QB3 calculations²¹) is lower than the TS1 energy required to initiate *aci*-rearrangement, this pathway requires no additional input energy and we can assume that any spontaneously-formed *aci*-nitro tautomer will lose OH before reaching the ion detector in our experiments. This result explains the high yield of $C_7H_6NO^+$ at negative time-delays in our experiments, which we assign to the $S = 1$ P2 product.

In addition to the spontaneous P2 formation pathway, Figure 10 also indicates three higher-energy pathways leading to different $C_7H_6NO^+$ structures that become accessible upon absorption of one probe photon (orange arrows) from either the vertical IP (i.e., by the parent molecular ion 2-NT⁺) or the *aci*-nitro tautomer with initial energy equal to that of TS1. Direct OH loss from INT2 can form either singlet ($S = 1$) or triplet ($S = 3$) $C_7H_6NO^+$ as structure P1 with energies 11.07 eV and 10.90 eV, respectively. The $S = 3$ product can

then cyclize with an additional 1.32 eV energy through TS2b to produce the cyclic P2 in the triplet state. These dissociation pathways, which are only accessible upon probe excitation, explain the presence of the T_3 timescale in the transient ion signals of the parent 2-NT⁺ and C₇H₆NO⁺, where the opposite signs of the corresponding amplitude coefficients (c in Tables 2 and 3) indicate that direct excitation of the parent ion can induce OH loss. As a result, the T_3 contribution to the C₇H₆NO⁺ signal in our experiments is expected to arise from both the singlet state P1 and triplet-state P1/P2 dissociation pathways.

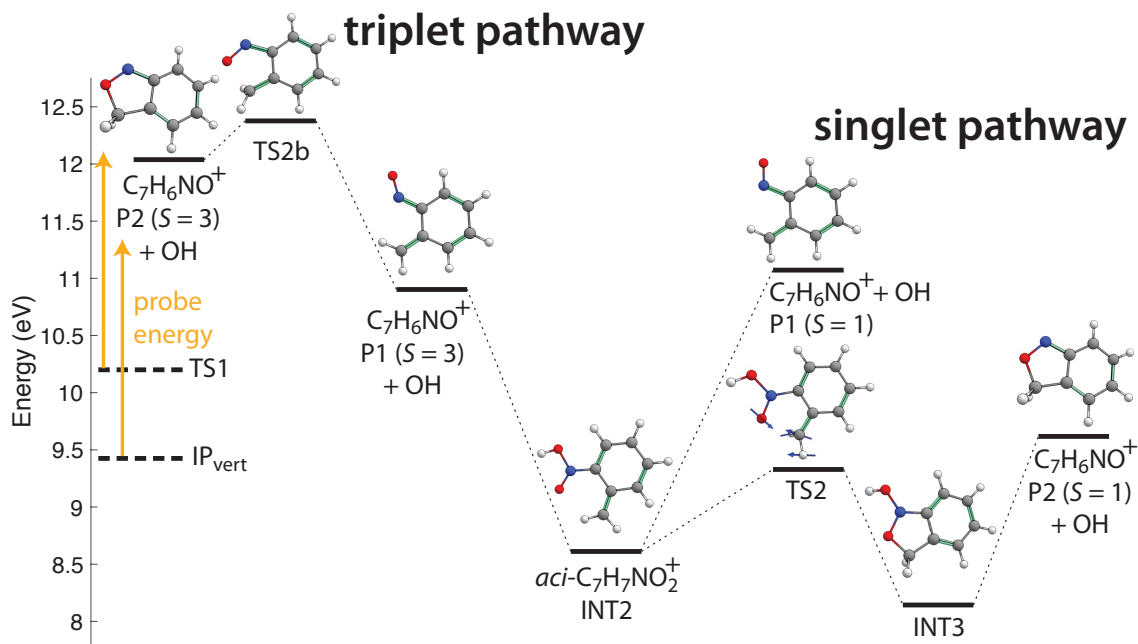


Figure 10: Mechanism of dissociation from the *aci*-nitro tautomer to C₇H₆NO⁺ products formed in the singlet and triplet states.

3.3.3 CO loss from C₇H₆NO⁺: Formation of C₆H₆N⁺

Finally, we turn to the CO loss pathway from C₇H₆NO⁺ to form C₆H₆N⁺. Previous theoretical studies examined CO loss from only the singlet C₇H₆NO⁺ product (P2, Figure 10), which indicated a large 2.61 eV dissociation barrier.²¹ We computed the CO loss pathways beginning from the P2 structures in both the singlet and triplet states (Figures 11(a) and (b), respectively, and Supporting Information, Figures S8 and S9).

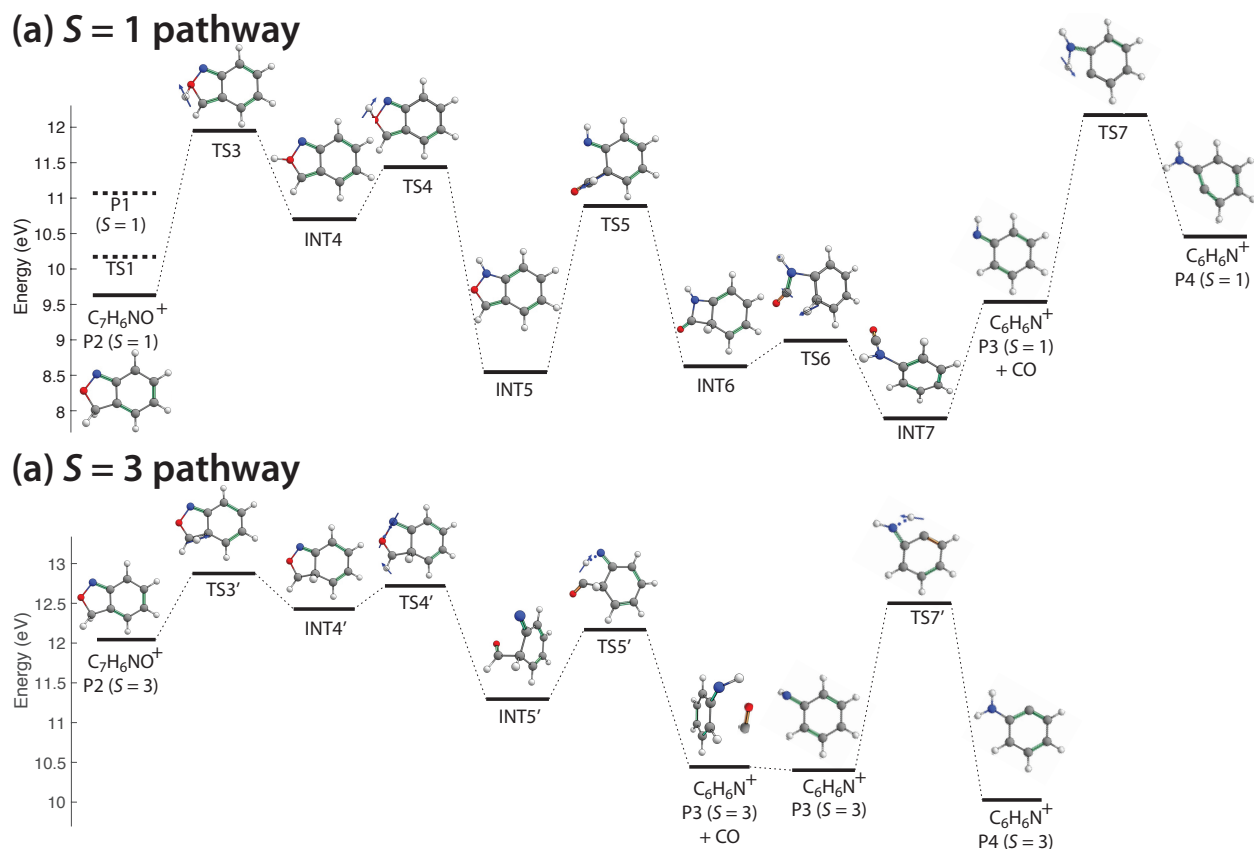


Figure 11: Mechanism of CO loss from $C_7H_6NO^+$ products P2 formed in (a) singlet and (b) triplet states.

In rough agreement with Ref.,²¹ the singlet $C_7H_6NO^+$ requires 2.32 eV to lose the CO moiety. These results indicate that the $C_7H_6NO^+$ formed via the lowest-energy singlet pathway in Figure 10 does not have enough energy to lose CO, even when taking into consideration the TS1 energy, as the energy barrier to reach TS3 is still 1.73 eV. In contrast, the singlet P1 that becomes accessible following absorption of a probe photon (dashed line, Figure 11(a)) only requires an extra 0.88 eV to induce a series of hydrogen atom migrations and internal rotations that leads to CO loss and production of the $C_6H_6N^+$ product P3 (Figure 11(a)). From the triplet P2, an additional energy input of 0.84 eV initiates a more direct CO loss pathway to form P3 in the triplet state (Figure 11(b)). We note that an additional higher-energy triplet dissociation pathway analogous to the singlet pathway in Figure 11(a) was also identified, as shown in the Supporting Information, Figures S10 and

S11. Collectively, these computed dissociation pathways suggest that the $C_7H_6NO^+$ formed in either the singlet or triplet state upon absorption of a probe photon can lose CO with little additional energy input. Therefore, both the observed T_3 relaxation timescale and oscillations in the $C_6H_6N^+$ fragment can both be attributed to excitation of the parent ion by the probe pulse.

3.4 Preservation of vibrational coherence in the *aci*-nitro tautomer

The distinct oscillatory dynamics observed in the $C_7H_6NO^+$ ion as compared to other ions (Figure 6) suggests that its precursor is a distinct structure from the parent 2-NT⁺. Coupled to the ADMP results in Figure 9 and previous pump-probe results on intramolecular H-atom attack in excited state neutrals,^{63,64} we propose that these oscillations arise from coherent vibrational dynamics in the *aci*-nitro tautomer of 2-NT⁺. The *aci*-nitro tautomer as structure INT1 is predicted to form as early as ~ 20 fs based on the ADMP results, and at least by ~ 60 fs based on earlier experiments.^{63,64} Therefore, INT1 is expected to be present for the dynamics recorded after 60 fs in Figure 6. The subsequent relaxation of INT1 to the more stable INT1r and INT2 structures is predicted to occur over the next several hundred fs. These *aci*-nitro tautomer structures are predicted to have higher-frequency torsional vibrations (86.9 cm^{-1} for INT1, 61.0 cm^{-1} for INT1r, and 79.8 cm^{-1} for INT2, Figure 12) than the 2-NT cation at 47.9 cm^{-1} . These results suggest that the faster 114 cm^{-1} oscillations observed in the $C_7H_6NO^+$ transient as compared to the 91 cm^{-1} oscillations of the parent 2-NT⁺ (Figure 6) may be attributed to the coherent torsional motion of the *aci*-nitro tautomer.

Additional insight into the dynamics of conversion from the initial INT1 *aci*-nitro tautomer to the INT1r and INT2 structures can be gained through analysis of the slowing oscillations of the $C_7H_6NO^+$ transient with increasing pump-probe delay as noted in Figure 6. The oscillatory component of the $C_7H_6NO^+$ signal from Figure 6 was fit to an exponen-

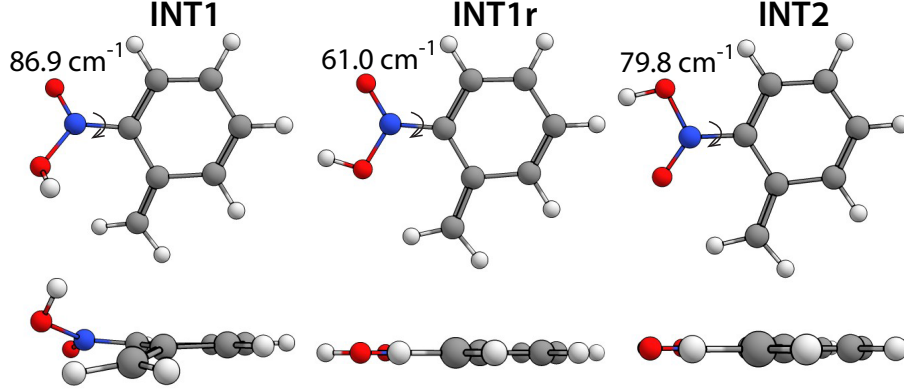


Figure 12: Aci structures.

tially decaying cosine function

$$S(\tau) = ae^{-\tau/T} \cos(2\pi f\tau + \phi), \quad (2)$$

with frequency $f = 115 \text{ cm}^{-1}$ and phase $\phi = -0.97 \text{ rad}$, as well as an exponentially decaying linearly chirped cosine function

$$S(\tau) = ae^{-\tau/T} \cos\left(2\pi \left[f_0\tau + \frac{1}{2}k\tau^2\right] + \phi_0\right), \quad (3)$$

with initial frequency $f_0 = 127 \text{ cm}^{-1}$, chirp rate $k = 0.972 \text{ ps}^{-2}$, and initial phase $\phi_0 = -1.22 \text{ rad}$.

The experimental $\text{C}_7\text{H}_6\text{NO}^+$ oscillatory signal fit to both eqs (2) (red) and (3) (blue) is shown in Figure 13. The dotted lines corresponding to the ion yield minima at 180 fs, 470 fs, and 780 fs match to within ± 2 fs of the minima in eq (3), while the second and third minima of eq (2) are 6 fs behind and 34 fs ahead of the experimental minima, respectively. The instantaneous frequency $f(\tau)$ according to eq (3) decreases from 121 cm^{-1} at 180 fs to 101 cm^{-1} at 780 fs. This 17% decrease in the instantaneous frequency is in between the $\sim 30\%$ frequency decrease between INT1 and INT1r and the 8% decrease between INT1 and INT2 seen in Figure 12. Although the expected errors in computed frequencies preclude a direct comparison between the experimental and computed frequencies, the observed frequency

decrease suggests that some mixture of INT1, INT1r, and INT2 structures are present by 780 fs after ionization.

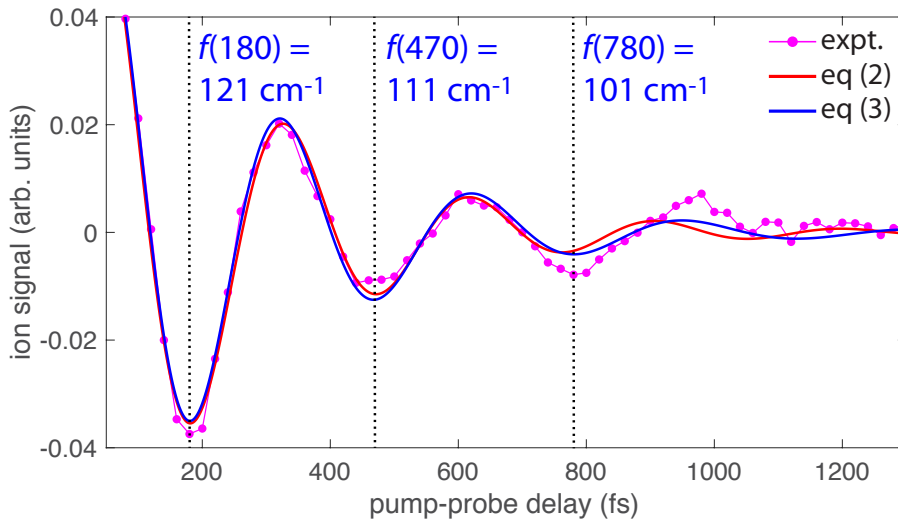


Figure 13: Oscillatory $\text{C}_7\text{H}_6\text{NO}^+$ ion signal (magenta dots) fit to eq (2) (red) and eq (3) (blue). Dotted lines indicate minima in the experimental ion yield.

The collective experimental and computational results discussed above provide substantial evidence that the observed slowing oscillations in the $\text{C}_7\text{H}_6\text{NO}^+$ product can be assigned to the coherent torsional motion of the *aci*-nitro tautomer and its conversion from the initially formed INT1 to more stable structures. This finding indicates that the initially-prepared vibrational coherence in the parent 2-NT^+ ion is preserved following the H-atom attack that forms the *aci*-nitro tautomer. To the best of our knowledge, this result is the first report of conserved vibrational coherence upon intramolecular rearrangement **in a radical cation, and builds on the results of Ref. ⁶⁴ showing conserved vibrational coherence following H-atom transfer in neutral excited 2-(2'-Hydroxyphenyl)benzothiazole.** Previous studies have reported conserved vibrational coherence following internal conversion in excited cyclohexadiene,⁶⁵ benzonitriles,^{66,67} Rydberg states of *N*-methyl morpholine,^{60,61} and azobenzene radical cation.³⁸ CO loss from excited-state metal hexacarbonyls has also been reported to result in coherent vibrational motion of the remaining metal pentacarbonyl.⁶⁸⁻⁷⁰ We attribute this unexpected behavior to the exceptionally fast H-atom attack within $\sim 20 - 60$

fs, which maintains the localized vibrational excitation along the torsional coordinate.

3.5 Summary of 2-NT⁺ rearrangement and dissociation dynamics

The experimental and theoretical results presented in the previous sections are combined to form our current understanding of 2-NT⁺ rearrangement and dissociation dynamics, presented in Figure 14. The black structure denotes the *aci*-nitro tautomer intermediate, while the colored structures correspond to the products indicated in Figures 3, 5, and 6. The colored arrows denote excitation by the pump (dark red) or probe (orange), the solid black arrows denote reaction pathways computed in Section 3.3, and the dotted arrows denote additional proposed pathways towards observed dissociation products. The reaction pathways labeled **I** through **IV** are summarized below.

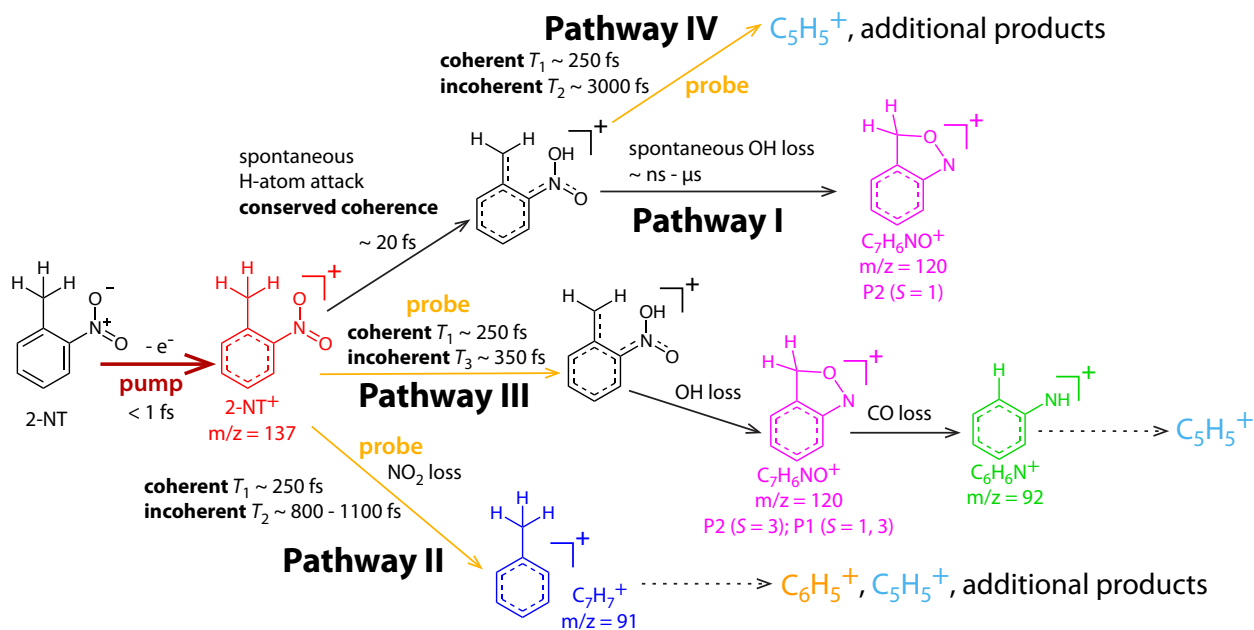


Figure 14: tentative dissociation pathway scheme

First, the pump pulse ionizes 2-NT to produce 2-NT⁺. In the absence of probe pulse excitation, a significant fraction of the ions produced undergo no further dissociation, producing the large peak at m/z = 137 seen in Figure 3(a) at negative time-delay and denoted as the red parent ion in Figure 14. Much of the remaining parent ion population has sufficient energy

to overcome the *aci*-rearrangement energy barrier of 0.76 eV (Figure 8), which produces the *aci*-nitro tautomer as structure INT1 (Figure 8) as early as ~ 20 fs according to our ADMP simulations (Figure 9). The calculated reaction pathway shown in Figure 10 indicates that the *aci*-nitro tautomer is expected to spontaneously lose OH to form $C_7H_6NO^+$ at $m/z = 120$ (magenta) via Pathway **I** in Figure 14. This pathway produces exclusively $C_7H_6NO^+$ structure P2 with $S = 1$ (Figure 10). The high yield of $m/z = 120$ at negative time delays (Figure 3) is consistent with Pathway **I** requiring no probe excitation.

We next consider the pathways induced by excitation of the parent 2-NT⁺ (red in Figure 14) structure with the probe pulse. Probe excitation can induce direct NO₂ loss from the parent ion to produce $C_7H_7^+$ ($m/z = 91$, blue, Pathway **II**). This direct dissociation pathway occurs following coherent probe excitation on the T_1 timescale of ~ 250 fs based on the observed oscillations, as well as the incoherent T_2 timescale of 800 – 1100 fs (Tables 2 and 3). The $C_7H_7^+$ may further dissociate to form $C_6H_5^+$, $C_5H_5^+$, and other smaller products. In particular, the nearly perfect antiphase oscillations of $C_6H_5^+$ with the parent ion suggest that the coherent Pathway **II** can form this product. The additional sequential dissociation Pathway **III** involves first *aci*-rearrangement induced by probe excitation, followed by OH loss to form $C_7H_6NO^+$ (magenta) as structure P1 with $S = 1, 3$ and/or P2 with $S = 3$ (Figure 10). A portion of this excited $C_7H_6NO^+$ undergoes subsequent CO loss to form $C_6H_6N^+$ (green). These species arise from an incoherent excitation pathway on the T_3 timescale of ~ 350 fs and could be formed as either singlet or triplet products (Figures 10 - 11). It is worth noting that the $C_6H_6N^+$ product also exhibits antiphase oscillations with the same frequency as the parent ion, suggesting that coherent excitation on the T_1 timescale can also initiate dissociation via Pathway **III**. However, the lack of corresponding oscillations at the same frequency and phase in the $C_7H_6NO^+$ product suggests that the coherently excited parent ion undergoes the full sequential dissociation shown in Pathway **III** to form $C_6H_6N^+$. Finally, the presence of the T_3 timescale in the $C_5H_5^+$ ion suggests that the $C_6H_6N^+$ can undergo further dissociation to form this product.

Finally, we consider the interaction of the spontaneously-formed *aci*-nitro tautomer with the probe pulse (Pathway **IV**). The coherent dynamics of this species discussed in Section 3.4 indicate that one or more dissociation products can be formed upon its coherent excitation. Based on the observed $C_5H_5^+$ oscillations being close to antiphase with the $C_7H_6NO^+$ (Figure 6), it is likely that $C_5H_5^+$ is a significant product of *aci*-nitro tautomer excitation. Additionally, the observation that the oscillations in the $m/z = 91$ product (assigned to $C_7H_7^+$) are somewhat shifted from antiphase with the parent ion suggests that an additional product with this m/z value, i.e., $C_6H_5N^+$, may be formed by excitation of the *aci*-nitro tautomer. The presence of small amounts of $m/z = 89$ and 90 (likely $C_6H_3N^+$ and $C_6H_4N^+$) observable in Figure 3 suggests that such dissociation pathways involving the loss of one or more H atoms are possible.

4 Conclusion

Coherent vibrational dynamics in 2-NT radical cation were probed with strong-field adiabatic ionization with near-infrared pulses and cation excitation with visible pulses. Observed oscillations in ion yields with the pump-probe delay was attributed to the coherent excitation of the C–NO₂ torsional motion in the parent 2-NT cation. This vibrational coherence was found to be preserved upon spontaneous H-atom attack to form the *aci*-nitro tautomer based on the faster oscillations in the $C_7H_6NO^+$ ion formed by –OH loss from the *aci*-nitro tautomer structure. A series of DFT calculations both supported the assertion of preserved coherence in the *aci*-nitro tautomer and determined the H-atom attack mechanism involving three *aci*-nitro tautomer structures. The subsequent –OH and –CO loss pathways from the *aci*-nitro tautomer determined through DFT calculations found that these dissociation reactions could produce both singlet and triplet $C_7H_6NO^+$ products. Collectively, these results provide a detailed picture of the coherent and incoherent excitation pathways in 2-NT radical cation that lead to the formation of multiple dissociation products. Future

high-level calculations of ground- and excited-state potential energy surfaces in 2-NT cation and the *aci*-nitro tautomer, along with additional time-resolved measurements with different probe wavelengths, could provide further insight into the specific excited states accessed by the coherent excitation pathways observed in this work. Building on the present results, such additional studies could help develop efficient coherent control schemes for 2-NT and other nitroaromatic energetic molecules.

Acknowledgement

The authors acknowledge the support of the U.S. Army Research Office through Contract W911NF-18-1-0051 (KMT) and the U.S. Department of Energy, Office of Basic Energy Sciences, Division of Materials Sciences and Engineering under Award DE-FG02-96ER45579 (PJ).

Supporting Information Available

Laser pulse characterization, additional pump-probe data, tabulated theoretical results, magnified structures of intermediates, transition states, and dissociation products.

References

- (1) Rajasekharan Pillai, V. N. Photoremovable Protecting Groups in Organic Synthesis. *Synthesis* **1980**, *1980*, 1–26.
- (2) Gao, X.; Gulari, E.; Zhou, X. In Situ Synthesis of Oligonucleotide Microarrays. *Biopolymers* **2004**, *73*, 579–596.
- (3) Ellis-Davies, G. C. R. Caged Compounds: Photorelease Technology for Control of Cellular Chemistry and Physiology. *Nat. Methods* **2007**, *4*, 619–628.

- (4) Sikder, A.; Sikder, N. A Review of Advanced High Performance, Insensitive and Thermally Stable Energetic Materials Emerging for Military and Space Applications. *J. Hazard. Mater.* **2004**, *112*, 1 – 15.
- (5) Weickhardt, C.; Tönnies, K. Short Pulse Laser Mass Spectrometry of Nitrotoluenes: Ionization and Fragmentation Behavior. *Rapid Commun. Mass Spectrom.* **2002**, *16*, 442–446.
- (6) McEnnis, C.; Dikmelik, Y.; Spicer, J. B. Femtosecond Laser-Induced Fragmentation and Cluster Formation Studies of Solid Phase Trinitrotoluene Using Time-of-Flight Mass Spectrometry. *Appl. Surf. Sci.* **2007**, *254*, 557 – 562.
- (7) Sulzer, P.; Rondino, F.; Ptasinska, S.; Illenberger, E.; Märk, T. D.; Scheier, P. Probing Trinitrotoluene (TNT) by Low-Energy Electrons: Strong Fragmentation Following Attachment of Electrons Near 0 eV. *Int. J. Mass Spectrom.* **2008**, *272*, 149 – 153.
- (8) Mullen, C.; Coggiola, M. J.; Oser, H. Femtosecond Laser Photoionization Time-of-Flight Mass Spectrometry of Nitro-Aromatic Explosives and Explosives Related Compounds. *J. Am. Soc. Mass Spectrom.* **2009**, *20*, 419–429.
- (9) Cohen, R.; Zeiri, Y.; Wurzburg, E.; Kosloff, R. Mechanism of Thermal Unimolecular Decomposition of TNT (2,4,6-Trinitrotoluene): A DFT Study. *J. Phys. Chem. A* **2007**, *111*, 11074–11083.
- (10) Wang, B.; Wright, D.; Cliffel, D.; Haglund, R.; Pantelides, S. T. Ionization-Enhanced Decomposition of 2,4,6-Trinitrotoluene (TNT) Molecules. *J. Phys. Chem. A* **2011**, *115*, 8142–8146.
- (11) Van, B. N.; Nikolaeva, E.; Shamov, A.; Khrapkovskii, G.; Tsyshevsky, R. Exploration of Decomposition Pathways of 2,4,6-Trinitrotoluene (TNT) Radical Ions by Means of Density Functional Theory. *Int. J. Mass Spectrom.* **2015**, *392*, 7 – 15.

- (12) Furman, D.; Kosloff, R.; Zeiri, Y. Mechanism of Intact Adsorbed Molecules Ejection Using High Intensity Laser Pulses. *J. Phys. Chem. C* **2016**, *120*, 11306–11312.
- (13) Beynon, J. H.; Saunders, R. A.; Topham, A.; Williams, A. E. The Dissociation of o-Nitrotoluene Under Electron Impact. *J. Chem. Soc.* **1965**, *0*, 6403–6405.
- (14) Shao, J.-D.; Baer, T. The Dissociation Dynamics of Energy Selected o-Nitrotoluene Ions. *Int. J. Mass Spectrom. Ion Process.* **1988**, *86*, 357 – 367.
- (15) Choe, J. C.; Kim, M. S. Photodissociation Kinetics of the P-Nitrotoluene Molecular Ion on a Nanosecond Time Scale. *J. Phys. Chem.* **1991**, *95*, 50–56.
- (16) Simeonsson, J. B.; Lemire, G. W.; Sausa, R. C. Trace Detection of Nitrocompounds by ArF Laser Photofragmentation/Ionization Spectrometry. *Appl. Spectrosc.* **1993**, *47*, 1907–1912.
- (17) Kosmidis, C.; Marshall, A.; Clark, A.; Deas, R. M.; Ledingham, K. W. D.; Singhal, R. P.; Harris, F. M. Multiphoton Ionization and Dissociation of Nitrotoluene Isomers by UV Laser Light. *Rapid Commun. Mass Spectrom.* **1994**, *8*, 607–614.
- (18) Kosmidis, C.; Ledingham, K. W. D.; Kilic, H. S.; McCanny, T.; Singhal, R. P.; Langley, A. J.; Shaikh, W. On the Fragmentation of Nitrobenzene and Nitrotoluenes Induced by a Femtosecond Laser at 375 nm. *J. Phys. Chem. A* **1997**, *101*, 2264–2270.
- (19) Lozovoy, V. V.; Zhu, X.; Gunaratne, T. C.; Harris, D. A.; Shane, J. C.; Dantus, M. Control of Molecular Fragmentation Using Shaped Femtosecond Pulses. *J. Phys. Chem. A* **2008**, *112*, 3789–3812.
- (20) Zhang, Q.; Fang, W.; Xie, Y.; Cao, M.; Zhao, Y.; Shan, X.; Liu, F.; Wang, Z.; Sheng, L. Photoionization and Dissociation Study of P-Nitrotoluene: Experimental and Theoretical Insights. *J. Mol. Struct.* **2012**, *1020*, 105 – 111.

- (21) Cao, M.; Li, Y.; Chu, G.; Chen, J.; Shan, X.; Liu, F.; Wang, Z.; Sheng, L. VUV Photoionization and Dissociation of o-Nitrotoluene: Experimental and Theoretical Insights. *J. Electron. Spectros. Relat. Phenomena* **2013**, *191*, 41 – 47.
- (22) Ampadu Boateng, D.; Gutsev, G. L.; Jena, P.; Tibbetts, K. M. Dissociation Dynamics of 3- and 4-Nitrotoluene Radical Cations: Coherently Driven C–NO₂ Bond Homolysis. *J. Chem. Phys.* **2018**, *148*, 134305.
- (23) Wettermark, G. Photochromism of o-Nitrotoluenes. *Nature* **1962**, *194*, 677.
- (24) Chen, S. C.; Xu, S. C.; Diao, E.; Lin, M. C. A Computational Study on the Kinetics and Mechanism for the Unimolecular Decomposition of o-Nitrotoluene. *J. Phys. Chem. A* **2006**, *110*, 10130–10134.
- (25) Fayet, G.; Joubert, L.; Rotureau, P.; Adamo, C. A Theoretical Study of the Decomposition Mechanisms in Substituted o-Nitrotoluenes. *J. Phys. Chem. A* **2009**, *113*, 13621–13627.
- (26) Gudem, M.; Hazra, A. Intersystem Crossing Drives Photoisomerization in o-Nitrotoluene, a Model for Photolabile Caged Compounds. *J. Phys. Chem. A* **2018**, *122*, 4845–4853.
- (27) Schmierer, T.; Laimgruber, S.; Haiser, K.; Kiewisch, K.; Neugebauer, J.; Gilch, P. Femtosecond Spectroscopy on the Photochemistry of Ortho-Nitrotoluene. *Phys. Chem. Chem. Phys.* **2010**, *12*, 15653–15664.
- (28) Fröbel, S.; Gilch, P. Femtochemistry of Selected Di-Substituted Benzenes. *J. Photochem. Photobiol. A* **2016**, *318*, 150 – 159.
- (29) Pearson, B.; Nichols, S.; Weinacht, T. Molecular Fragmentation Driven by Ultrafast Dynamic Ionic Resonances. *J. Chem. Phys.* **2007**, *127*, 131101.

- (30) Nichols, S.; Weinacht, T.; Rozgonyi, T.; Pearson, B. Strong-Field Phase-Dependent Molecular Dissociation. *Phys. Rev. A* **2009**, *79*, 043407.
- (31) Gonzalez-Vazquez, J.; Gonzalez, L.; Nichols, S. R.; Weinacht, T. C.; Rozgonyi, T. Exploring Wavepacket Dynamics Behind Strong-Field Momentum-Dependent Photodissociation in CH₂BrI⁺. *Phys. Chem. Chem. Phys.* **2010**, *12*, 14203–14216.
- (32) Geißler, D.; Marquetand, P.; González-Vázquez, J.; González, L.; Rozgonyi, T.; Weinacht, T. Control of Nuclear Dynamics with Strong Ultrashort Laser Pulses. *J. Phys. Chem. A* **2012**, *116*, 11434–11440.
- (33) Zhu, X.; Lozovoy, V. V.; Shah, J. D.; Dantus, M. Photodissociation Dynamics of Acetophenone and Its Derivatives with Intense Nonresonant Femtosecond Pulses. *J. Phys. Chem. A* **2011**, *115*, 1305–1312.
- (34) Konar, A.; Shu, Y.; Lozovoy, V. V.; Jackson, J. E.; Levine, B. G.; Dantus, M. Polyatomic Molecules under Intense Femtosecond Laser Irradiation. *J. Phys. Chem. A* **2014**, *118*, 11433–11450.
- (35) Bohinski, T.; Tibbetts, K. M.; Tarazkar, M.; Romanov, D. A.; Matsika, S.; Levis, R. J. Strong Field Adiabatic Ionization Prepares a Launch State for Coherent Control. *J. Phys. Chem. Lett.* **2014**, *5*, 4305–4309.
- (36) Tibbetts, K. M.; Tarazkar, M.; Bohinski, T.; Romanov, D. A.; Matsika, S.; Levis, R. J. Controlling the Dissociation Dynamics of Acetophenone Radical Cation Through Excitation of Ground and Excited State Wavepackets. *J. Phys. B: At. Opt. Mol. Phys.* **2015**, *48*, 164002.
- (37) Ho, J.-W.; Chen, W.-K.; Cheng, P.-Y. Femtosecond Pump-Probe Photoionization-Photofragmentation Spectroscopy: Photoionization-Induced Twisting and Coherent Vibrational Motion of Azobenzene Cation. *J. Chem. Phys.* **2009**, *131*, 134308.

- (38) Munkerup, K.; Romanov, D.; Bohinski, T.; Stephansen, A. B.; Levis, R. J.; Sølling, T. I. Conserving Coherence and Storing Energy during Internal Conversion: Photoinduced Dynamics of cis- and trans-Azobenzene Radical Cations. *J. Phys. Chem. A* **2017**, *121*, 8642–8651.
- (39) Ampadu Boateng, D.; Gutsev, G. L.; Jena, P.; Tibbetts, K. M. Ultrafast Coherent Vibrational Dynamics in Dimethyl Methylphosphonate Radical Cation. *Phys. Chem. Chem. Phys.* **2018**, *20*, 4636–4640.
- (40) Lezius, M.; Blanchet, V.; Rayner, D. M.; Villeneuve, D. M.; Stolow, A.; Ivanov, M. Y. Nonadiabatic Multielectron Dynamics in Strong Field Molecular Ionization. *Phys. Rev. Lett.* **2001**, *86*, 51–54.
- (41) Lezius, M.; Blanchet, V.; Ivanov, M. Y.; Stolow, A. Polyatomic Molecules in Strong Laser Fields: Nonadiabatic Multielectron Dynamics. *J. Chem. Phys.* **2002**, *117*, 1575–1588.
- (42) Ampadu Boateng, D.; Tibbetts, K. M. Measurement of Ultrafast Vibrational Coherences in Polyatomic Radical Cations with Strong-Field Adiabatic Ionization. *JoVE* **2018**, *138*, e58263.
- (43) Gutsev, G. L.; Ampadu Boateng, D.; Jena, P.; Tibbetts, K. M. A Theoretical and Mass-Spectrometry Study of Dimethyl Methylphosphonate: New Isomers and Cation Decay Channels in an Intense Femtosecond Laser Field. *J. Phys. Chem. A* **2017**, *121*, 8414–8424.
- (44) Kane, D. J.; Trebino, R. Characterization of Arbitrary Femtosecond Pulses Using Frequency-Resolved Optical Gating. *IEEE J. Quant. Electron.* **1993**, *29*, 571–579.
- (45) Hankin, S. M.; Villeneuve, D. M.; Corkum, P. B.; Rayner, D. M. Intense-Field Laser Ionization Rates in Atoms and Molecules. *Phys. Rev. A* **2001**, *64*, 013405.

- (46) Frisch, M.; Trucks, G.; Schlegel, H.; Scuseria, G.; Robb, M.; Cheeseman, J.; Scalmani, G.; Barone, V.; Mennucci, B.; Petersson, G.; et al, Gaussian 09, Revision B. 01. 2016.
- (47) Krishnan, R.; Binkley, J. S.; Seeger, R.; Pople, J. A. Self-Consistent Molecular Orbital Methods. XX. A Basis Set for Correlated Wave Functions. *J. Chem. Phys.* **1980**, *72*, 650–654.
- (48) Montgomery, J. A.; Frisch, M. J.; Ochterski, J. W.; Petersson, G. A. A Complete Basis Set Model Chemistry. VI. Use of Density Functional Geometries and Frequencies. *J. Chem. Phys.* **1999**, *110*, 2822–2827.
- (49) Burke, K.; Perdew, J. P.; Wang, Y. In *Electronic Density Functional Theory: Recent Progress and New Directions*; Dobson, J. F., Vignale, G., Das, M. P., Eds.; Springer US: New York, 1998; pp 81–111.
- (50) Becke, A. D. Density Functional Thermochemistry. III. The Role of Exact Exchange. *J. Chem. Phys.* **1993**, *98*, 5648–5652.
- (51) Lee, C.; Yang, W.; Parr, R. G. Development of the Colle-Salvetti Correlation-Energy Formula into a Functional of the Electron Density. *Phys. Rev. B* **1988**, *37*, 785–789.
- (52) Yanai, T.; Tew, D. P.; Handy, N. C. A New Hybrid Exchange–Correlation Functional Using the Coulomb-Attenuating Method (CAM-B3LYP). *Chem. Phys. Lett.* **2004**, *393*, 51 – 57.
- (53) Chai, J.-D.; Head-Gordon, M. Long-Range Corrected Hybrid Density Functionals with Damped Atom-Atom Dispersion Corrections. *Phys. Chem. Chem. Phys.* **2008**, *10*, 6615–6620.
- (54) Head-Gordon, M.; Pople, J. A.; Frisch, M. J. MP2 Energy Evaluation by Direct Methods. *Chem. Phys. Lett.* **1988**, *153*, 503 – 506.

- (55) Bauernschmitt, R.; Ahlrichs, R. Treatment of Electronic Excitations Within the Adiabatic Approximation of Time Dependent Density Functional Theory. *Chem. Phys. Lett.* **1996**, *256*, 454 – 464.
- (56) NIST Standard Reference Database 69. <http://webbook.nist.gov/chemistry/>, <http://webbook.nist.gov/chemistry/>. Last checked 10/05/18.
- (57) Montgomery, J. A.; Frisch, M. J.; Ochterski, J. W.; Petersson, G. A. A Complete Basis Set Model Chemistry. VII. Use of the Minimum Population Localization Method. *J. Chem. Phys.* **2000**, *112*, 6532–6542.
- (58) Fukui, K. The Path of Chemical Reactions - The IRC Approach. *Acc. Chem. Res.* **1981**, *14*, 363–368.
- (59) Schlegel, H. B.; Iyengar, S. S.; Li, X.; Millam, J. M.; Voth, G. A.; Scuseria, G. E.; Frisch, M. J. Ab Initio Molecular Dynamics: Propagating the Density Matrix with Gaussian Orbitals. III. Comparison with Born–Oppenheimer Dynamics. *J. Chem. Phys.* **2002**, *117*, 8694–8704.
- (60) Waters, M. D. J.; Skov, A. B.; Larsen, M. A. B.; Clausen, C. M.; Weber, P. M.; Sølling, T. I. Symmetry Controlled Excited State Dynamics. *Phys. Chem. Chem. Phys.* **2019**, DOI: 10.1039/C8CP05950K, in press.
- (61) Zhang, Y.; Jónsson, H.; Weber, P. M. Coherence in Nonradiative Transitions: Internal Conversion in Rydberg-Excited N-methyl and N-ethyl Morpholine. *Phys. Chem. Chem. Phys.* **2017**, *19*, 26403–26411.
- (62) Shishkov, I. F.; Vilkov, L. V.; Kovács, A.; Hargittai, I. Molecular Geometry of 2-Nitrotoluene from Gas Phase Electron Diffraction and Quantum Chemical Study. *J. Mol. Struct.* **1998**, *445*, 259 – 268.

- (63) Herek, J. L.; Pedersen, S.; Bañares, L.; Zewail, A. H. Femtosecond Real-Time Probing of Reactions. IX. Hydrogen-Atom Transfer. *J. Chem. Phys.* **1992**, *97*, 9046–9061.
- (64) Lochbrunner, S.; Wurzer, A. J.; Riedle, E. Ultrafast Excited-State Proton Transfer and Subsequent Coherent Skeletal Motion of 2-(2'-Hydroxyphenyl)benzothiazole. *J. Chem. Phys.* **2000**, *112*, 10699–10702.
- (65) Kosma, K.; Trushin, S. A.; Fuß, W.; Schmid, W. E. Cyclohexadiene Ring Opening Observed with 13 fs Resolution: Coherent Oscillations Confirm the Reaction Path. *Phys. Chem. Chem. Phys.* **2009**, *11*, 172–181.
- (66) Yatsushashi, T.; Trushin, S.; Fuß, W.; Rettig, W.; Schmid, W.; Zilberg, S. Ultrafast Charge Transfer and Coherent Oscillations in 4-Piperidino-Benzonitrile. *Chem. Phys.* **2004**, *296*, 1 – 12.
- (67) Fuß, W.; Schmid, W. E.; Kuttan Pushpa, K.; Trushin, S. A.; Yatsushashi, T. Ultrafast Relaxation and Coherent Oscillations in Aminobenzonitriles in the Gas Phase Probed by Intense-Field Ionization. *Phys. Chem. Chem. Phys.* **2007**, *9*, 1151–1169.
- (68) Trushin, S.; Fuß, W.; Schmid, W. Conical Intersections, Pseudorotation and Coherent Oscillations in Ultrafast Photodissociation of Group-6 Metal Hexacarbonyls. *Chem. Phys.* **2000**, *259*, 313 – 330.
- (69) Trushin, S.; Kosma, K.; Fuß, W.; Schmid, W. Wavelength-Independent Ultrafast Dynamics and Coherent Oscillation of a Metal–Carbon Stretch Vibration in Photodissociation of Cr(CO)₆ in the Region of 270–345 nm. *Chem. Phys.* **2008**, *347*, 309 – 323.
- (70) Kosma, K.; Trushin, S. A.; Fuß, W.; Schmid, W. E.; Schneider, B. M. R. Photodissociation of Group-6 Hexacarbonyls: Observation of Coherent Oscillations in an Antisymmetric (Pseudorotation) Vibration in Mo(CO)₅ and W(CO)₅. *Phys. Chem. Chem. Phys.* **2010**, *12*, 13197–13214.

TOC Graphic

